applied sciences

MDPI

Article

Transient Cooling of Millisecond-Pulsed Heat Sources by a Jet Impingement Heat Sink with Metallic Phase Change Material

Liang Chen *, Qi Wang, Yansong Si and Yu Hou

State Key Laboratory of Multiphase Flow in Power Engineering, Xi'an Jiaotong University, Xi'an 710049, China
* Correspondence: liangchen@mail.xjtu.edu.cn

Abstract: Thermal management has become a critical issue for the reliable operation of electronic devices, especially for pulsed heat sources with high heat flux. The intense temperature rise in a short period puts forward high requirements on thermal management. In this work, a heat sink combining the confined jet impingement with metallic phase change material (PCM) is proposed for the thermal management of millisecond-pulsed heat sources. A transient model is established to simulate the conjugated heat transfer. The heat transfer characteristics of a jet impingement heat sink and the temperature responses under millisecond heat pulses are obtained, and the effects of jet structure and metallic PCM thickness on the cooling performance are analyzed. Results show that the jet impingement with a jet diameter of 2 mm and an impingement height of 2 mm can achieve effective cooling on a 3 × 3.5 mm^2 heat source, and the surface temperature is 62.2 °C for a constant power density (150 W/cm^2). Under the millisecond heat pulses with a peak power density of 600 W/cm^2 and a duty cycle of 0.25, the temperature on the heating surface fluctuates in the same period with the heat pulses, and the maximum temperature reaches 66.9 °C for a heat sink without metallic PCM. An appropriate PCM thickness should be smaller than 0.1 mm so that the phase change can be cycled within heat pulse intervals, and the maximum temperature can be maintained around the phase change temperature (61.5 °C).

Keywords: jet impingement cooling; metallic PCM; liquid cooling; heat sink; millisecond heat pulses

check for updates

Citation: Chen, L.; Wang, Q.; Si, Y.; Hou, Y. Transient Cooling of Millisecond-Pulsed Heat Sources by a Jet Impingement Heat Sink with Metallic Phase Change Material. *Appl. Sci.* **2023**, *13*, 1812. https://doi.org/10.3390/app13031812

Academic Editor: Shiwei Zhang

Received: 17 November 2022
Revised: 4 January 2023
Accepted: 8 January 2023
Published: 31 January 2023

Copyright: © 2023 by the authors. Licensee MDPI, Basel, Switzerland. This article is an open access article distributed under the terms and conditions of the Creative Commons Attribution (CC BY) license (https://creativecommons.org/licenses/by/4.0/).

1. Introduction

With the development of super-large-scale integration, industrial electrical equipment, and consumer electronic products, the power density of electronic devices has been increasing, and the requirements for thermal management techniques are becoming higher [1,2]. As the temperature of electronic devices increases by 10 °C, the safety and reliability of their normal operation will decrease by 50%. Therefore, thermal management has become a critical issue for the reliable operation of electronic devices, especially for pulsed heat sources with high heat flux. The intense temperature rise in a short period puts forward high requirements on thermal management.

Jet impingement cooling is one of the effective approaches to solving the heat dissipation problem of high-power electronic devices. As the high-speed liquid or gas impinges onto the heater surface, a much thinner velocity boundary layer can be formed than the channel flow, which helps to reduce the heat transfer resistance of forced convection. Jet impingement cooling is preferred when strong cooling is required on a local area of the heating surface. The liquid cooling medium can achieve better cooling performance than the gas medium for jet impingement, especially for confined jet impingement. If the jet space is small enough, the influence of gravity and other volumetric forces can be negligible, and the confined jet impingement is suitable for applications in automotive, airborne, and microgravity environments [3].

Many factors can influence the heat transfer performance of jet impingement cooling, such as the geometrical structure of the jet (shape of the jet, jet height H, jet diameter

d, depth of the nozzle l, jet spacing S, etc.), jet velocity, jet direction, physical properties of cooling medium, surface structure to be cooled, etc. For single-phase confined jet impingement, many studies have been performed on the heat transfer characteristics of single jet and multiple jets [4–10]. Generally speaking, the cooling performance of single-phase jet impingement improves with the increase in jet Re number and the decrease in d. When H/d is in the range of $1 < H/d < 5$, H has no obvious effects on the heat transfer coefficient; when H/d is too large, the heat transfer performance tends to degrade. With the same pump power and flow rate, the average heat transfer coefficient decreases with the increase in S/d, while the heat transfer coefficient of the stagnation point changes little.

For devices with transient power fluctuations, phase change materials (PCMs) can be used as an auxiliary temperature control method [11–13]. During the thermal design process, the corresponding active cooling system can be designed in the light of the basic heat load of the device, and PCMs can be equipped to prevent the device from overheating during the transient power fluctuation. Without the phase change temperature control unit, the cooling system needs to be designed according to the highest heat load, increasing its cost and complexity. In recent years, metallic PCMs have been paid wide attention in the field of thermal management [14–18]. Metallic PCMs have high thermal conductivity, low volume change rate, and no phase separation, phase stratification or evaporation, which provides an effective solution for thermal management.

DW Yoo et al. [19] studied the performance of plate-fin and pin-fin heat sinks combining a metallic PCM for intermittent electronic equipment. The PCM was a Wood alloy (50Bi/27Pb/13Sn/10Cd, melting temperature 70 °C). It was found that PCM could provide additional heat capacity and reduce the size of thermal management equipment and energy consumption compared to conventional heat sinks. Gaofeng Hao et al. [20] integrated metallic PCM into an IGBT molybdenum plate and analyzed the effects of incorporating PCM on normal working devices by the finite method. The results showed that the heat pulse handling ability of the devices incorporated with metallic PCM was improved significantly. PCM integrated into the heat sink [21–23] can serve as a thermal buffer for longer power surges due to the larger volumes of PCM involved [24], while the thermal contact resistance between electronic devices and heat sinks has still not been solved. Another method is to embed the PCM into a substrate [25,26] or the interface between a heat sink and an electronics package, which has limited buffer ability due to the small acceptable PCM volumes but a favorable thermal contact performance [27,28].

In this paper, the thermal performance of a jet impingement heat sink with metallic phase change material (PCM) is investigated for the thermal management of millisecond-pulsed heat sources. A transient model is established to simulate the conjugated heat transfer. The heat transfer characteristics of the jet impingement heat sink and the temperature responses under millisecond heat pulses are obtained, and the effects of jet structure and PCM thickness on the cooling performance are analyzed. The results show that a thin layer of metallic PCM is required for the cooling of millisecond-pulsed heat sources and the peak temperature can be reduced by 5.4 °C under a peak heat flux of 600 W/cm^2.

2. Numerical Methodology

2.1. Geometry Model

The total size of the heating surface was 72 mm × 50 mm, and eight 3 mm × 3.5 mm chips were arranged along the central line of the length direction. The chips were millisecond-pulsed heat sources, and pulse period was 4 ms, peak heat flux was 600 W/cm^2 with a cycle duty of 0.25. The average heat flux in other areas was about 1.2 W/cm^2. A heat sink combining the confined jet impingement with metallic PCM was proposed for the cooling of the local high heat flux of millisecond pulses. The metallic PCM was embedded between the contact surface of chips and the heat sink to reduce the temperature rise under the high heat flux pulses using the heat storage capacity of phase change. The jet impingement was used to remove the heat from the PCM.

Numerical models were established to study the cooling performance of the heat sink under the millisecond heat pulses. Firstly, a three-dimensional (3D) jet impingement model without a PCM layer was built, and the effects of geometrical parameters on the heat transfer characteristics were studied. The heat pulses were averaged over a cycle as a constant heat source. Considering the symmetry of the heat sink structure, 1/4 of the jet structure was selected as the simulation domain with a footprint area of 25 mm × 4.5 mm. As shown in Figure 1a, the gray part is the solid region (aluminum), and the blue part is the fluid region (glycol solution with a freezing point of −65 °C). A transient model was constructed to study the temperature responses of the heat sink under millisecond heat pulses and the effects of metallic PCM thickness. The simulation of the transient phase change model greatly increases the computational cost. To reduce the calculation time, the 3D model was simplified to a two-dimensional (2D) axisymmetric model as shown in Figure 1b and its validation is presented in Section 3.2.1. The red part shown in Figure 1b is metallic PCM and its area covers the entire chip with high heat flux.

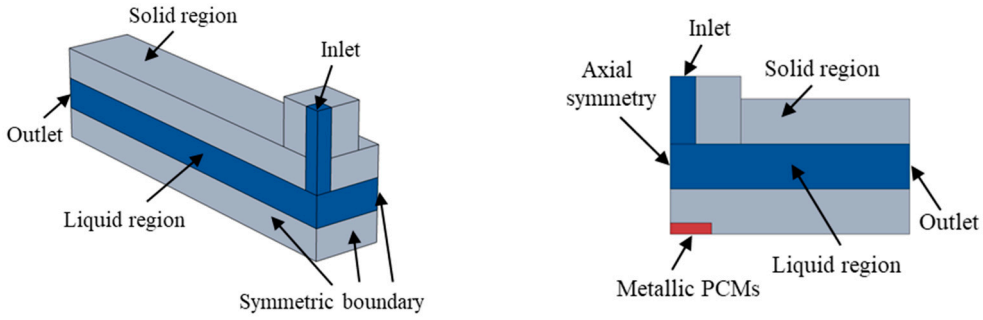


Figure 1. Numerical calculation geometry models: (**a**) 3D; (**b**) 2D axisymmetric.

2.2. Model Assumptions and Governing Equations

The following assumptions were made to simplify the simulation model.

(1) The flow and temperature fields are symmetric with respect to the geometric symmetry planes of the heat sink;
(2) The cooling medium is an incompressible fluid, and its thermophysical properties are adopted at the average temperature of the inlet and outlet;
(3) As the temperature of the device will not exceed 100 °C, the thermal radiation of the device to the external environment is negligible;
(4) The influence of gravity is negligible;
(5) The metallic PCM is assumed to be uniformly embedded between the contact surface of chips and the heat sink;
(6) Convection heat transfer of the melted PCM can be assumed to be negligible due to the small thickness.

Potthast F et al. [29] gave a critical *Re* number of 980 for the axial jet and 625 for the radial jet, and the critical *Re* number is related to the jet geometry. Revill [30] mentioned that a free jet is fully turbulent for jet *Re* number above approximately 1000~2000 and laminar for *Re* number below about 100. According to these studies, it is considered that all the jet flows are turbulent in this paper. In the current numerical calculation of engineering turbulence, the most widely used method is the Reynolds-averaged Navier–Stokes (RANS) method. Combined with the above assumptions, the following governing equations need to be satisfied for incompressible jet impingement [31,32].

Continuity equation

$$\frac{\partial}{\partial x_i}(u_i) = 0 \tag{1}$$

Momentum equation

$$\frac{\partial}{\partial t}(\rho u_i) + \frac{\partial}{\partial x_j}(\rho u_i u_j) = -\frac{\partial p}{\partial x_i} + \frac{\partial}{\partial x_j}\left(\mu\frac{\partial u_i}{\partial x_j} - \rho\overline{u_i' u_j'}\right) \tag{2}$$

Energy equation

$$\frac{\partial}{\partial t}(\rho T) + \frac{\partial}{\partial x_j}(\rho T u_j) = \frac{\partial}{\partial x_j}\left(\frac{\mu}{Pr}\frac{\partial T}{\partial x_j} - \rho\overline{T' u_j'}\right) \tag{3}$$

where, u is the instantaneous velocity, m/s; i, j represent three coordinate direction identifiers; ρ is the fluid density, kg/m^3; μ is the dynamic viscosity of fluid, kg·m^{-1}·s^{-1}; Pr is the Prandtl number of fluid; and $-\rho\overline{u_i' u_j'}$ and $\rho\overline{T' u_j'}$ are the additional terms containing pulsations generated after time homogenization, called Reynolds stress and specific turbulent heat flux, respectively.

To close the above RANS equations, it is necessary to connect the additional terms of turbulence pulsation values with the homogenization equation values, that is, to introduce the turbulence model. Choosing a suitable turbulence model is very important to improve the reliability of numerical calculations. The k-ω turbulence model in COMSOL Multiphysics software is based on the Wilcox revised k-ω model [33], which takes into account the low Reynolds number, compressibility and predicts the propagation rate of free shear flow. It performs well in internal flow problems and calculates more accurately flows with strong curvature, separated flow, adverse pressure gradient, jet, and other phenomena. Therefore, the k-ω model was selected. For the near-wall surface processing, the automatic wall treatment was adopted, which can switch between low Reynolds number processing and wall function processing according to the grid resolution and obtain more accurate results with strong robustness.

The apparent Heat Capacity Method is used to model phase transition processes in metallic PCM, where the PCM heat capacity is given as a temperature-dependent function [34,35]. By solving a single heat transfer equation with effective material properties for both phases, the apparent heat capacity formula provides implicit capturing of the phase transition interface. The latent heat is taken into account by modifying the heat capacity [36]. This method has been used to simulate the solid–liquid phase change processes in many studies and has been proven to be effective [37–39]. It is assumed that the phase transition occurs in a temperature interval between T_{lower} ($T_{lower} = T_m - \Delta T/2$) and T_{upper} ($T_{upper} = T_m + \Delta T/2$). In the temperature interval, the phase state is expressed by a smooth function, θ, which represents the liquid fraction and is equivalent to 0 before T_{lower} and to 1 after T_{upper}. The expressions of the density (ρ) and the specific enthalpy (H^{th}) are as follows.

$$\rho = (1-\theta)\rho_1 + \theta\rho_2 \tag{4}$$

$$H^{th} = \frac{1}{\rho}\left((1-\theta)\rho_1 H_1^{th} + \theta\rho_2 H_2^{th}\right) \tag{5}$$

where, subscripts 1 and 2 indicate the material phase before or after transition, respectively. Differentiating with respect to temperature and after some equation transformations, the specific heat capacity is as follows:

$$C_p = \frac{\partial H^{th}}{\partial T} = \frac{1}{\rho}\left((1-\theta)\rho_1 C_{p,1} + \theta\rho_2 C_{p,2}\right) + \left(H_2^{th} - H_1^{th}\right)\frac{d\alpha_m}{dT} = C_{eq} + C_L \tag{6}$$

where, C_{eq} represents the equivalent heat capacity and C_L represents the distribution of latent heat (L), α_m represents the mass fraction and is defined by

$$\alpha_m = \frac{1}{2}\frac{\theta\rho_2 - (1-\theta)\rho_1}{(1-\theta)\rho_1 + \theta\rho_2} \tag{7}$$

The C_L is approximated by

$$C_L(T) = L\frac{d\alpha_m}{dT} \tag{8}$$

The total heat released per unit volume during the phase change coincides with L as follows.

$$\int_{T_{lower}}^{T_{upper}} C_L(T)dT = L\int_{T_{lower}}^{T_{upper}} \frac{d\alpha_m}{dT}dT = L \tag{9}$$

Therefore, the apparent heat capacity (C_p) applied in the heat equation is expressed by

$$C_p = \frac{\partial H^{th}}{\partial T} = \frac{1}{\rho}\left((1-\theta)\rho_1 C_{p,1} + \theta\rho_2 C_{p,2}\right) + L \tag{10}$$

The effective thermal conductivity and the effective density are as follows.

$$k = (1-\theta)k_1 + \theta k_2 \tag{11}$$

$$\rho = (1-\theta)\rho_1 + \theta\rho_2 \tag{12}$$

The metallic PCM used in this work was a 49Bi/21In/18Pb/12Sn alloy whose mean temperature of the phase change (T_m) was 58 °C, and its thermophysical properties are shown in Table 1.

Table 1. The thermophysical properties of the 49Bi/21In/18Pb/12Sn alloy [14,40].

Thermophysical Properties	Solid	Liquid
ρ (kg/m^3)	9060	8200
C_p (J·kg^{-1}·K^{-1})	323	721
k (W·m^{-1}·K^{-1})	33.2	10.6
$\Delta T/2$ (K)	1.5	
L (J/kg)	28,980	

According to the symmetry assumption and the selection of calculation region, the geometric central planes were defined as symmetrical boundaries. The coolant inlet temperature was 35 °C, and the inlet volumetric flow rate (Q_V) of the single jet was 0.32 L/min. The outlet gauge pressure was 0. The boundary heat source was set for the area where the 3 × 3.5 mm^2 chip was located, and the heat flux (q'') was 150 W/cm^2 for the simulation cases of constant heat flux. q'' was set to be 1.2 W/cm^2 for the rest area around the chip. For the heat transfer interface, the other boundaries were defined as adiabatic boundaries, and the initial temperature of all areas was 35 °C.

2.3. Mesh Generation and Model Validation

Unstructured mesh was used, and the mesh of the fluid boundary region and chip region were refined. The heat sink with a jet height (H) of 2 mm and a square-edged jet diameter (d) of 2 mm was selected for the mesh independence tests. Models were simulated with different numbers of meshes including 26,718, 68,546, 127,091, 323,075, and 998,199. The maximum temperature of the heat sink bottom ($T_{\max}$) and the pressure drop (ΔP) were compared to evaluate the convergence with increasing mesh number. The criterion $\left|\left(X^j - X^{j+1}\right)/X^j\right| < 1 \times 10^{-3}$ was chosen for the mesh independence test, where X^j is the computed value of the variable for the current mesh and X^{j+1} is the value of the same variable after mesh refinement. The results are shown in Table 2. To ensure calculation accuracy and minimize computing costs, the mesh density of mesh 4 was selected for the meshing scheme of other structures.

Table 2. Results of the mesh independence test.

Mesh	Number of Cells	T_{max} /°C	$\left\|(T_{max}{}^{j} - T_{max}{}^{j+1})/T_{max}{}^{j}\right\|$	ΔP /Pa	$\left\|\left(\Delta P^{j} - \Delta P^{j+1}\right)/\Delta P^{j}\right\|$
Mesh1	26,718	63.83	6.75×10^{-3}	196.11	3.68×10^{-1}
Mesh2	68,546	63.39	1.27×10^{-2}	268.35	1.70×10^{-1}
Mesh3	127,091	62.59	5.67×10^{-3}	222.79	2.75×10^{-2}
Mesh4	323,075	62.24	6.11×10^{-4}	228.93	2.81×10^{-4}
Mesh5	998,199	62.20	—	229.00	—

Garimella S.V. et al. [4,6,41] carried out confined jet impingement experiments with water as the cooling medium. The parameters in the experiments were as follows: the jet diameter (d) was 1.59~12.7 mm, the Reynold number (Re) was 4000~23,000, and the ratio of jet height to jet diameter (H/d) was 1~5. Based on the experimental data, the heat transfer correlation was proposed for the Nusselt number of jet stagnation point (Nu_0). Under the corresponding experimental conditions, a two-dimensional axisymmetric model for the confined jet impingement was constructed, and the relevant settings of the model were the same as above. The simulation conditions were all within the applicable range of the correlation. The results of Nu_0 determined by the numerical simulation and the experimental correlation are shown in Figure 2. The calculation values of Nu_0 were in good agreement with the values predicted by experimental correlation, and the deviations were within ±10%.

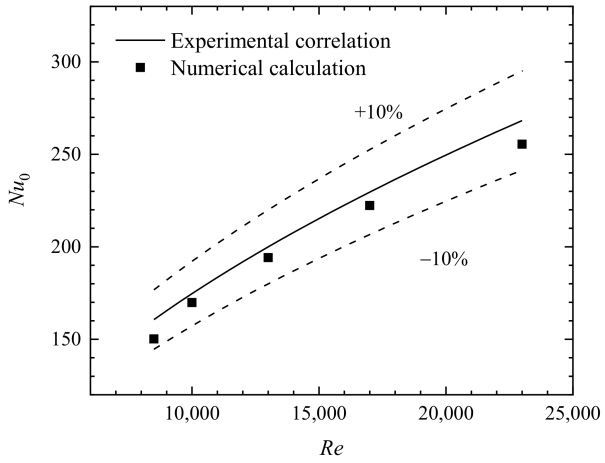


Figure 2. Comparison of Nu_0 determined by the numerical calculation and the correlation.

3. Results and Discussion

3.1. The Performance of Jet Impingement under a Constant Heat Load

Figure 3 shows the velocity contour and streamlines of confined jet impingement when H is 2 mm and d is 2 mm. Taking this working condition as an example, the flow and heat transfer characteristics of confined jet impingement are described. According to the velocity characteristics, the confined jet area can be divided into two parts: the stagnation area and the wall jet area. In the stagnation area, the velocity changes sharply from the axial direction to the radial direction, and the momentum and energy change significantly, showing a strong heat transfer capability. In the wall jet area, the working fluid shows a decelerated flow and its velocity decreases with the increase in radial distance. Vorticities are generated by violent impact and interference with other jets.

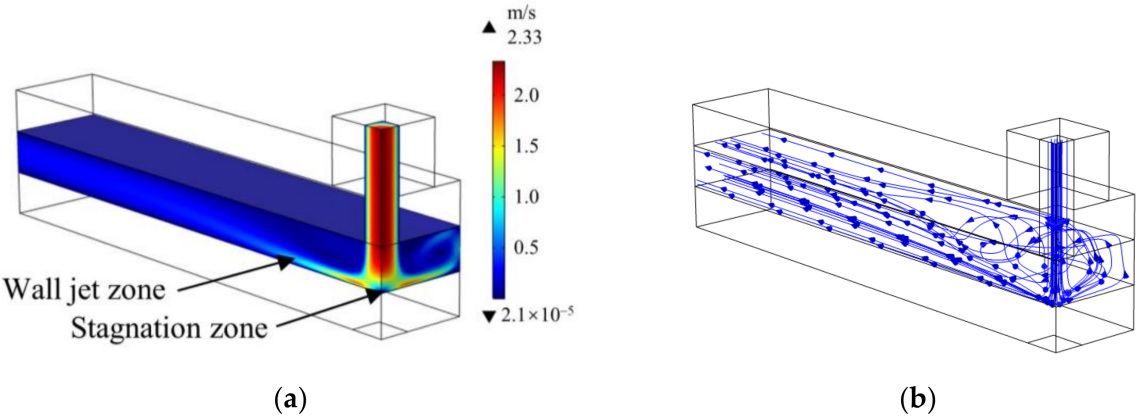
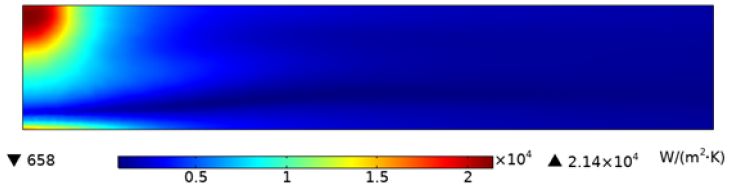


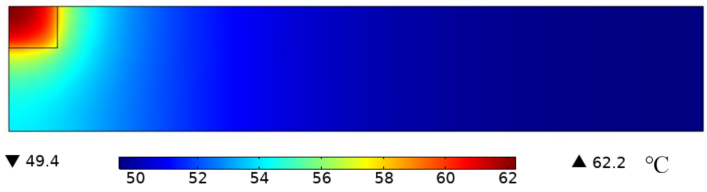
Figure 3. The velocity contour and streamlines of confined jet impingement: (**a**) Velocity distribution; (**b**) streamline distribution.

The distribution characteristics of the flow field affect the heat transfer of the impinged surface. Figure 4 shows the heat transfer coefficient (h) distribution on the impinged surface, the temperature (T) distribution on the heat sink bottom, and the variations of h and T along the symmetric line. As seen in the figure, h at the stagnation area is much higher than that at other areas due to the strong disturbance caused by a sharp change in velocity. With the increase in radial distance, h decreases, and its distribution is approximately bell-shaped. The large h in the stagnation area exactly meets the requirement of high heat flux chip heat dissipation, and the lower h in the wall jet area is sufficient to satisfy the low power heat dissipation of areas around the chip. The temperature at the center of the chip is the highest and gradually decreases outwards. The maximum temperature of the heat sink bottom (T_{max}) is 62.2 °C, meaning the jet impingement can meet the heat dissipation requirements of the heating surface under the constant heat load (150 W/cm^2).

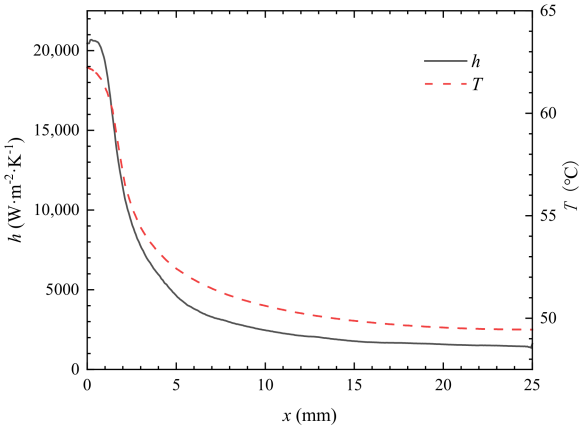
The heat sinks with different jet heights (H) were simulated with a specified jet diameter (d) of 2 mm. Considering the device's strict requirement on the size of heat dissipation space, the jet height studied is between 0.5 to 2.5 mm. Figure 5 shows variations of T_{max} and pressure drop (ΔP) with H. It can be seen that T_{max} increases with the increase in H, and the increase rate gradually decreases as H is larger than 1.5 mm, while the pressure drop ΔP has an opposite trend with the maximum temperature. As the coolant impinges into a confined space, the smaller the jet space, the stronger the disturbance near the impinged surface with the same jet velocity, leading to a better heat transfer performance but a higher pressure drop. However, the area influenced by jet impingement is limited, and the weakening effect on disturbance due to the increasing jet space decreases with the increasing jet height.



(**a**)



(**b**)



(**c**)

Figure 4. The distribution of heat transfer coefficient and temperature: (**a**) the heat transfer coefficient distribution of the jet impingement surface; (**b**) the temperature distribution of the heat sink bottom; (**c**) the heat transfer coefficient and temperature distribution of the symmetric line.

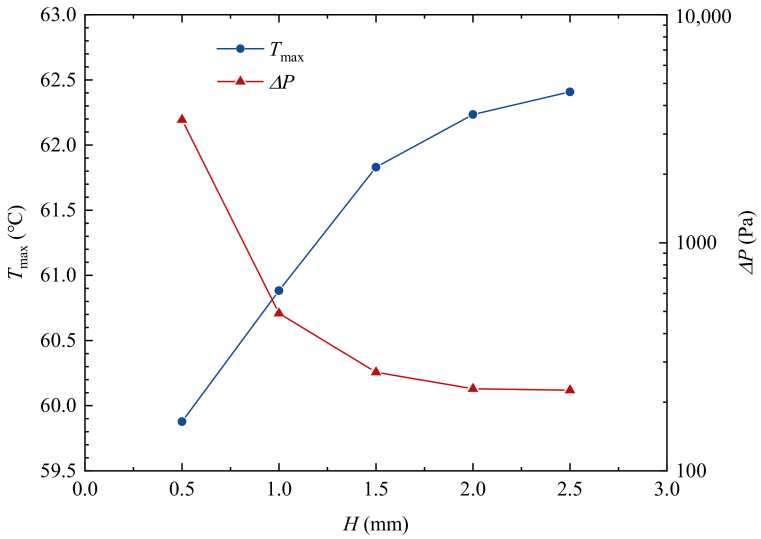


Figure 5. The relationship between T_{max}, ΔP and H when d = 2 mm.

When H is 1 mm and 2 mm, the structures with a jet diameter (d) between 0.5 mm and 2.5 mm were simulated, and the results are shown in Figure 6. With the decrease in d, the average inlet velocity (u_{ave}) and ΔP increase, T_{max} decreases, and the change rate gradually decreases. With the same d, the T_{max} when H is 2 mm is higher than that when H is 1 mm and ΔP is lower. Figure 7 shows the relationship between Re and Nu_0. It is known that with the increase in Re, Nu_0 increases. In addition, with the decrease in H, Nu_0 increases. The higher the inlet velocity and Re, the bigger the turbulence intensity, and the stronger the disturbance caused by the sharp change in velocity in the stagnation zone, meaning a higher Nu_0 and a better cooling performance can be achieved.

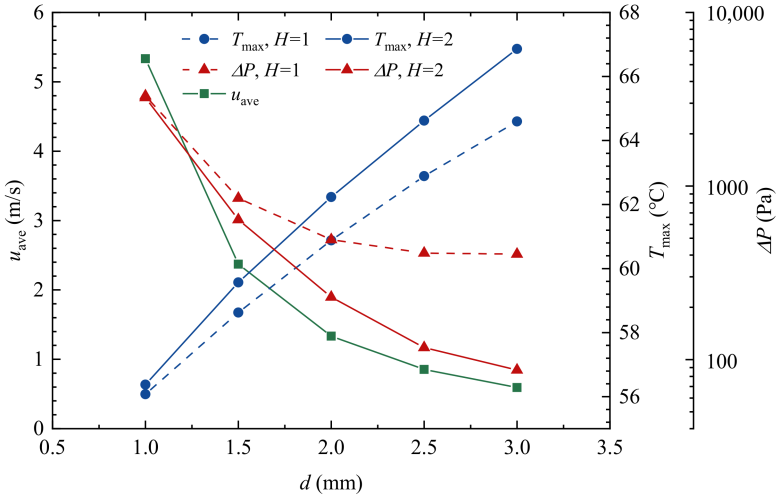


Figure 6. The relationship between u_{ave}, T_{max}, ΔP and d when H = 1 mm, 2 mm.

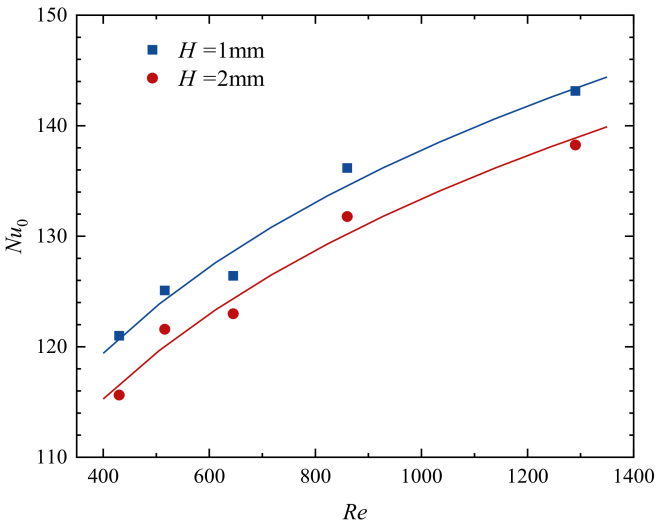


Figure 7. The relationship between Re and Nu_0 when H = 1 mm, 2 mm.

When H is 0.5 mm or d is 1 mm, the heat sink shows good cooling performance and T_{max} is much lower than other structures, but ΔP is also far higher than other structures. Although the heat transfer performance of jet impingement can be enhanced with the decrease in jet diameter d and jet height H, d and H should not be too small. In comparison, it is more appropriate to take d as 2 mm and H as 2 mm, which has good cooling performance as well as a moderate ΔP.

3.2. Transient Performance under High Heat Flux Millisecond Pulses

3.2.1. Transient Responses under Millisecond-Pulsed Heat Sources without PCM

Based on the results under a constant heat load, the three-dimensional transient model with the structure of d as 2 mm and H at 2 mm was built. The heat flux boundary condition of the 3 × 3.5 mm^2 chip was changed from constant heat flux to millisecond heat pulses to obtain the temperature responses of the heat sink without a phase change temperature control unit. To reduce the solution time, the transient model takes the steady-state result as the initial value. Figure 8 shows the variations in T_{max} under heat pulses. It can be seen that T_{max} fluctuates in the same period as the heat pulses. During the heat pulse interval, T_{max} decreases. When the heat pulse comes, T_{max} rises rapidly and reaches 66.9 °C, 4.7 °C higher than the steady state value of 62.2 °C. The high response temperature caused by high heat flux pulses is detrimental to the reliability of electronic devices. Therefore, it is necessary to add a phase change temperature control unit to reduce the response temperature.

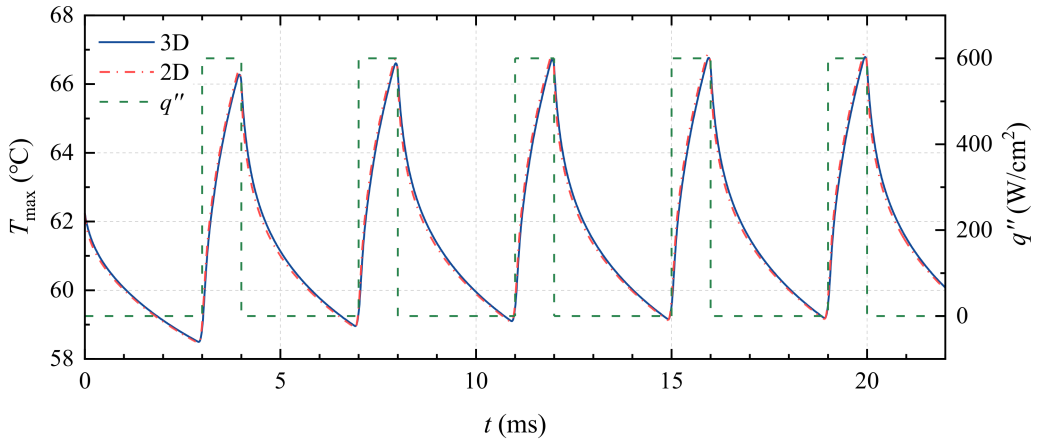


Figure 8. The variations in T_{max} under heat pulses without PCM.

The 2D axisymmetric model was used to calculate the transient responses with phase transition and its validity was verified first before calculation. The volumetric flow rate of the cooling medium and average inlet velocity of the 2D axisymmetric model are consistent with the 3D model. The chip area is equal to the chip area of 3 × 3.5 mm^2, and the other boundary conditions are similar to the 3D model. For the 2D axisymmetric model, the T_{max} under basic heat flux is 62.2 °C, which is the same as the 3D model. The transient result under the heat pulses is shown in Figure 8, and the initial value is also the result of the steady state. It can be seen from the figure that the variation trend of T_{max} of the 2D axisymmetric model is consistent with the 3D model. Therefore, the 2D axisymmetric model is effective and can be used to further study the temperature responses of the heat sink with metallic PCM.

3.2.2. The Effects of the Thickness of the Metallic PCM Layer

Metallic PCM can serve as a thermal buffer under heat pulses, but the effects of the PCM thicknesses on the cooling performance need to be further studied. When the filling thickness of PCM (δ) is 1 mm, the variations of T_{max} and the average phase change percentage of PCM (γ) are shown in Figure 9. It can be seen that during the calculation time, T_{max} rises to the mean temperature of the phase change (T_m = 58 °C), and is temporarily maintained around T_m, but then rises to a higher temperature quickly. The increase in the maximum T_{max} slows down as it increases beyond 110 °C, but γ continuously increases, indicating a steady state has not yet been reached. As the same trend of δ = 1 mm, When δ is 0.5 mm, T_{max} rises to T_m and is maintained around T_m temporarily. In addition, the time when T_{max} can be maintained around T_m is prolonged. After that, with the continuous increase in γ, T_{max} begins to rise, and the chip temperature cannot be kept within the allowed range.

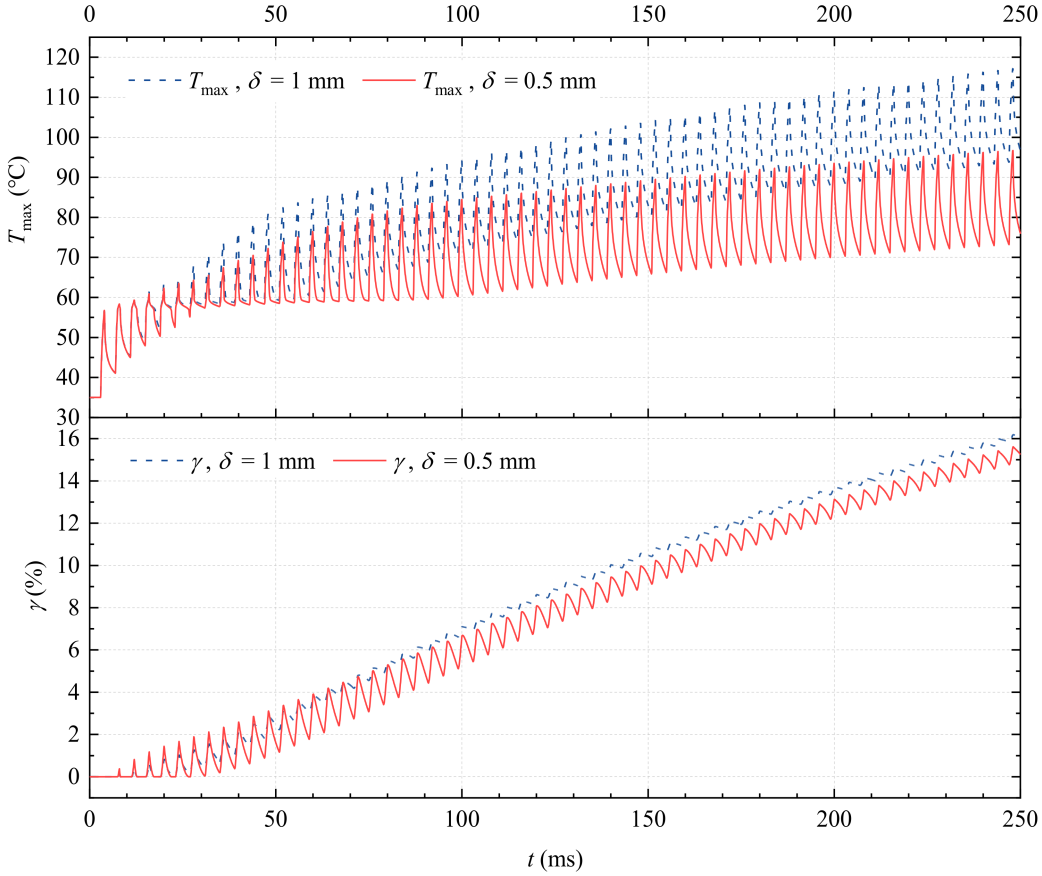


Figure 9. The variations in T_{max} and γ with time when δ = 1 mm, 0.5 mm.

Based on the above discussion on T_{max} and γ, it can be seen that T_{max} can be maintained around T_m if the metallic PCM can completely return to the solid state (γ = 0) before the next heat pulse. If the PCM cannot fully recover to the solid state (γ > 0) during the heat pulse interval, the metallic PCM adjacent to the heating surface will lose heat storage capability due to phase change. As the thermal conductivity of metallic PCM (33.2 $W \cdot m^{-1} \cdot K^{-1}$ for solid, 10.6 $W \cdot m^{-1} \cdot K^{-1}$ for liquid) is far less than aluminum (238 $W \cdot m^{-1} \cdot K^{-1}$), the heat cannot conduct away efficiently through the PCM within a short period. Therefore, the bottom temperature of the heat sink will start to rise when the next pulse comes.

According to the calculation results of δ at 1 mm and 0.5 mm, we can see that T_{max} can be maintained within a certain range for a longer time after reaching T_m with the decrease in δ. The results of T_{max} and γ when δ are 0.1 mm and 0.05 mm are shown in Figure 10. It can be seen from the figure that T_{max} and γ vary periodically when the thicknesses are 0.1 mm and 0.05 mm. The metallic PCM can be fully recovered to the solid state during heat pulse intervals, and T_{max} and γ have been stabilized within a short period. T_{max} can be maintained around T_m, and the maximum temperature is reduced from 66.9 °C to 61.8 °C when δ = 0.1 mm and 61.5 °C when δ = 0.05 mm. T_{max} changes little with the decrease in δ from 0.1 mm to 0.05 mm, but the maximum γ is increased from 6.7% to 11.4%, indicating a more effective utilization of PCM.

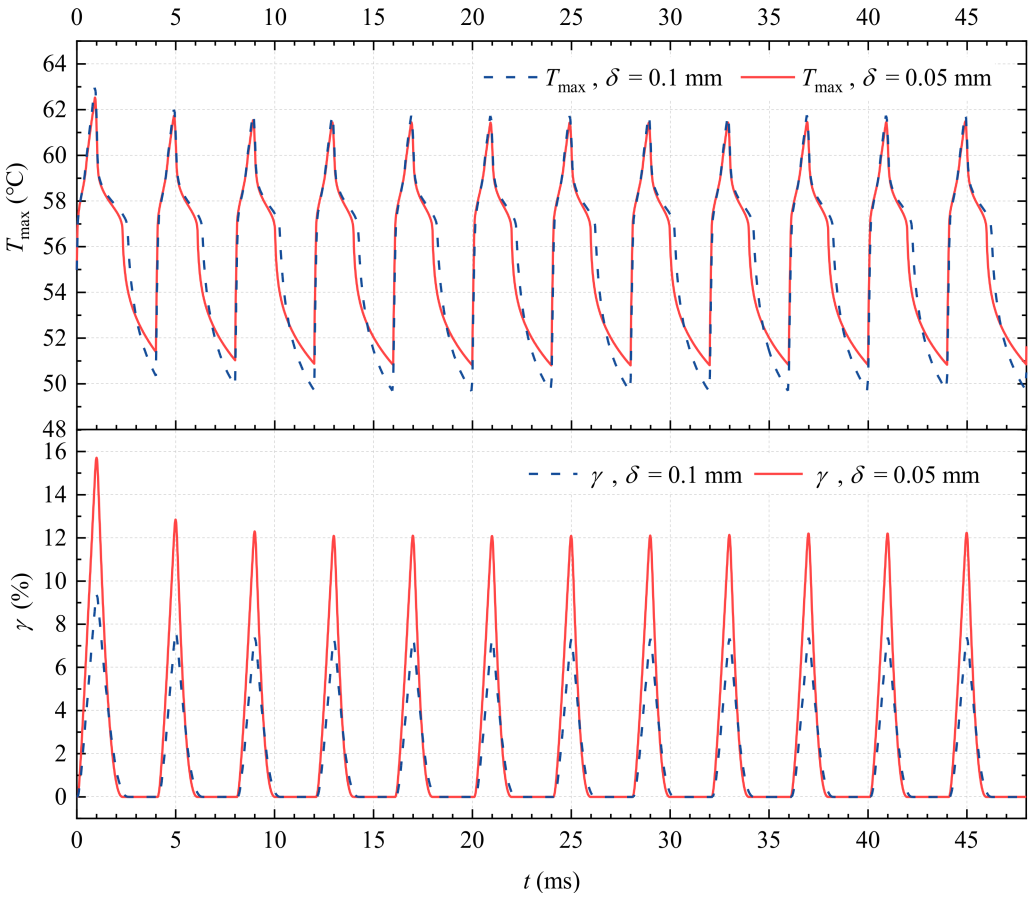


Figure 10. The variations in T_{max} and γ with time when δ = 0.1 mm, 0.05 mm.

Figure 11 shows the phase change process of the metallic PCM after reaching the periodic state when δ = 0.05 mm (corresponding to 44 ms~46.2 ms in Figure 10). The liquid fraction θ is 0 before the arrival of the heat pulse. During the heating period, the liquid fraction θ and phase change region increase rapidly, and then gradually decrease to 0 after the pulse. At the end of the heating period (45 ms), the phase change reaches its maximum, with a liquid fraction θ greater than 0.9 at the bottom and the thickness is about 0.005 mm. In the perpendicular direction, the phase change extends to 1/2 of the thickness, and the liquid fraction θ decreased with increasing thickness. It can also be seen that the phase change does not reach the periphery boundary even at the maximum γ, indicating that PCM with the same area of the heat source can work efficiently. The smaller melting area of PCM is due to the heat spreading from the heat source to the base of the heat sink, causing a lower heat flux and temperature in the marginal area.

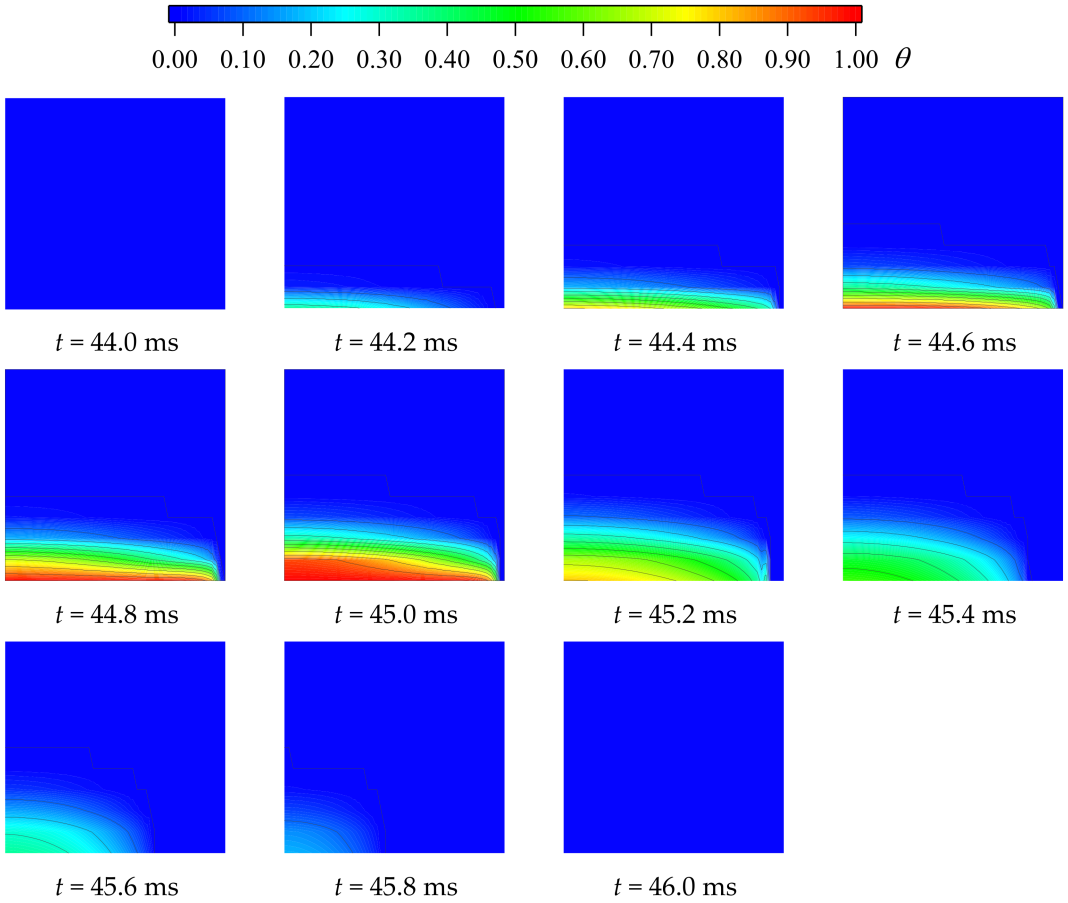


Figure 11. The phase change processes of metallic PCM during a heat pulse cycle.

Figure 12 shows the transient change in heat flux on the upper side of the metallic PCM during a heat pulse cycle (corresponds to 43~47 ms in Figure 10). Before the arrival of the heat pulse (43~44 ms as shown in Figure 12a), the heat flux on the upper side of the metallic PCM is maintained at approximately 20 W/cm^2, while the heat flux of the chip is 0. When the heat pulse hits (44~44.2 ms), the heat flux on the upper side of the metallic PCM rises rapidly, but the maximum heat flux is much less than the peak heat flux (600 W/cm^2) of the chip. During the heating period (44.2~45 ms as shown in Figure 12a), the heat flux decreases slightly due to the increase in liquid fraction. The heat flux in the central region is lower than the periphery region due to phase transition and the sudden drop in heat flux near the periphery boundary is due to the heat spreading from the heat source to the base of the heat sink. After the heat pulse (45~47 ms as shown in Figure 12b), the heat flux on the upper side of the metallic PCM decreases, and the area with high heat flux shrinks gradually. When the liquid fraction θ reduces to 0, the heat flux above metallic PCM also recovers to the value before the heat pulse. The change processes of heat flux above metallic PCM during a heat pulse cycle demonstrate the thermal buffer performance of metallic PCM.

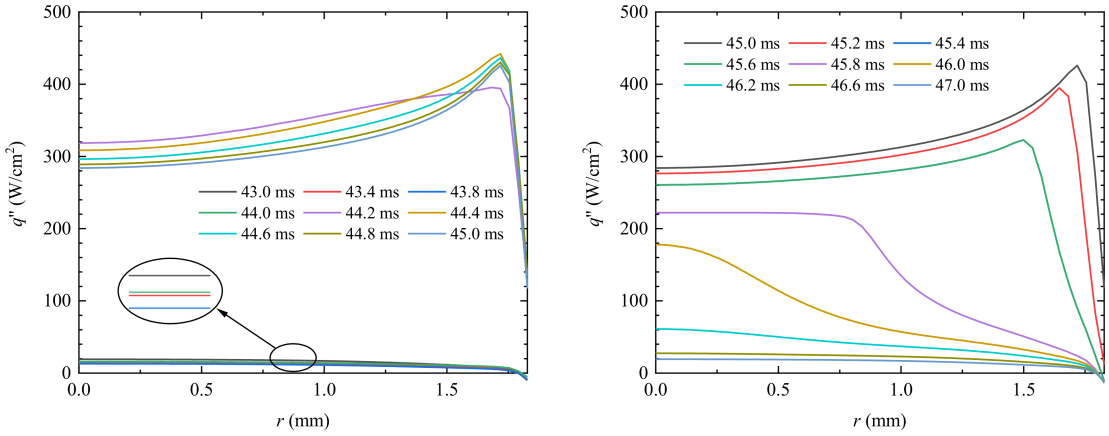


Figure 12. The change processes of heat flux on the upper side of the metallic PCM during a heat pulse cycle: (**a**) 43~45 ms, the duty period with heat flux of 600 W/cm^2 on the chip; (**b**) 45~47 ms, the idle period with zero heat flux on the chip.

3.2.3. The Effects of the Heat Pluses' Peak Heat Flux and Duty Cycle

Combined with the variations in T_{max} and the phase change process during a heat pulse cycle shown in Figures 10 and 11, it can be found that after reaching the melting point, the temperature increase rate is small when the underlying liquid fraction θ is small, while the temperature increases rapidly when the underlying PCM is almost complete phase change. Therefore, if the high heat flux lasts for a longer time, the buffer effect of the thin-layer PCM will not be obvious. With the same average heat flux and pulse period, the millisecond pulses with a peak heat flux of 300 W/cm^2 and a duty cycle of 0.5 were employed to study the buffer performance of the thin-layer PCM (δ = 0.05 mm) under low peak heat flux and large duty cycle pulse heating.

As shown in Figure 13, after reaching the periodic state, the temperature fluctuates in the same period as the heat pulses and rises for half of the cycle. T_{max} without PCM reaches 64.4 °C, 2.2 °C higher than the steady state value of 62.2 °C and 2.5 °C lower than the T_{max} (66.9 °C) of high peak heat flux and a short heating period. The use of a thin-layer metallic PCM makes the temperature decrease overall, and the highest T_{max} is 59.1 °C, which is 5.3 °C lower than that without PCM. At the initial moment of the pulse, the temperature increase rate with PCM is greater than that without PCM due to the lower thermal conductivity of the metallic PCM. When the temperature increases to the melting point, the temperature with PCM increases slower than that without PCM as a result of the latent heat. Then, with the expansion of the phase change region and the increase in the underlying liquid fraction θ, the temperature growth rate increases. As shown in Figure 14, compared with the high peak heat flux and short-period heating, the average phase change percentage γ decreases, but the phase change extends to more than 1/2 of the thickness in the perpendicular direction, and the region of the PCM bottom with high phase change degree is smaller, showing a better buffering performance. Therefore, low peak heat flux and large duty cycle pulse heating can take full advantage of metallic PCMs.

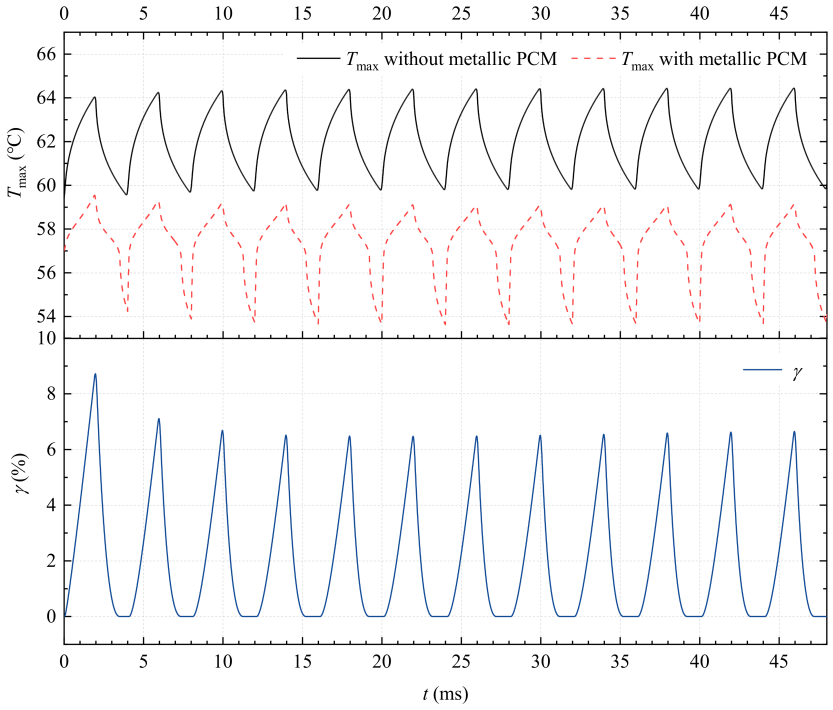


Figure 13. The variations in T_{max} and γ with time under low peak heat flux and large duty cycle pulses heating.

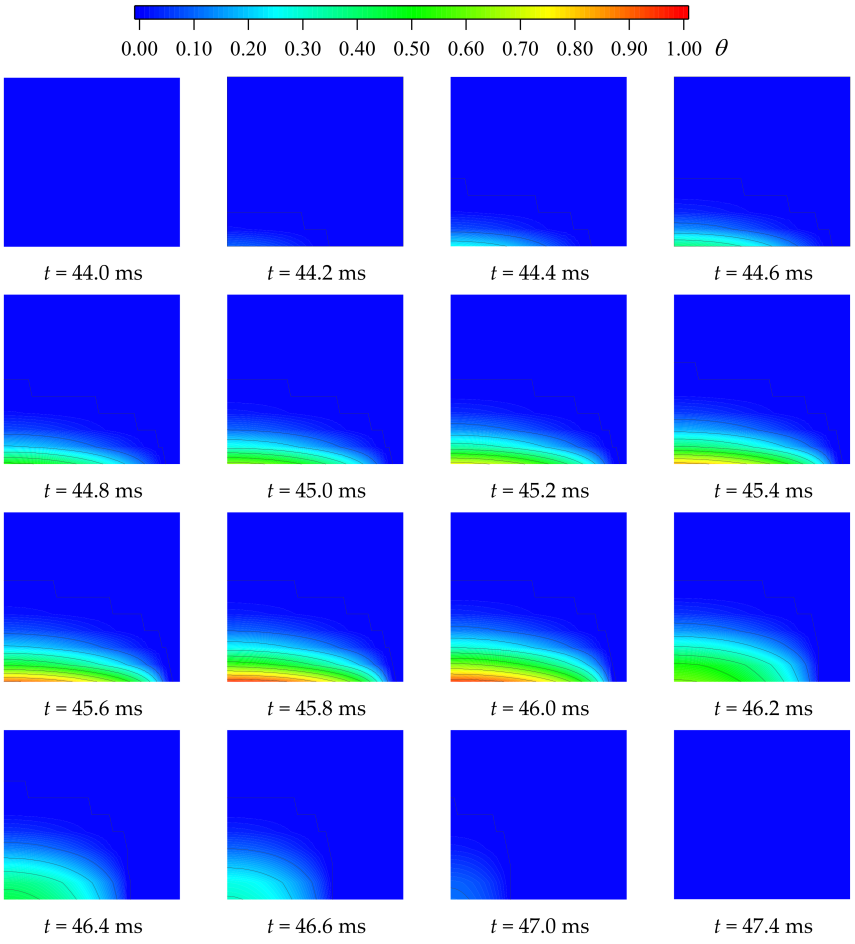


Figure 14. The phase change processes of metallic PCM during a heat pulse cycle under low peak heat flux and large duty cycle pulses heating.

3.2.4. The Comparison of Thermal Contact Performance between the Metallic PCM and Thermal Silicon Grease

Tight contact between the heating surface and heat-dissipating devices is required for effective heat management. In the studies above, the interface thermal resistance between the heat sink and the heating surface was not taken into consideration. Generally, thermal interface materials (TIMs) are used to fill the roughness of the coupled surfaces while eliminating the air with low thermal conductivity [42]. Thermal silicon grease is one of the traditional TIMs and has been widely used [43], while low melting point metal materials show several advantages owing to their unique properties [44]. The thin-layer metallic PCM embedded between the contact surface of the chips and the heat sink reacts as a TIM exactly when dealing with power surges, improving the thermal contact performance compared to the thermal silicon grease.

With the same filling area and thickness (0.05 mm) of the metallic PCM, the transient response under heat pluses of thermal silicon grease (thermal conductivity is 3 K/(m W)) is shown in Figure 15. The peak heat flux is 600 W/cm^2, and the duty cycle is 0.25. At the very beginning of the heating period, the temperature of both the thermal silicon grease and the metallic PCM rise rapidly until reaching the melting point of the PCM, the temperature of the metallic PCM increases slowly and is controlled around the melting point due to the phase change, while the temperature of the thermal silicon grease continues to increase at a high rate and reaches 119 °C, 57.5 °C higher than the metallic PCM. After the heating period, the temperature of the thermal silicon grease decreases rapidly, while the temperature of the metallic PCM shows a more moderate decreasing trend both during and after the solidification process due to its better thermal properties. Compared to the thermal silicon grease, metallic PCM can achieve a lower temperature and a smaller amplitude of fluctuations, showing a better thermal contact performance.

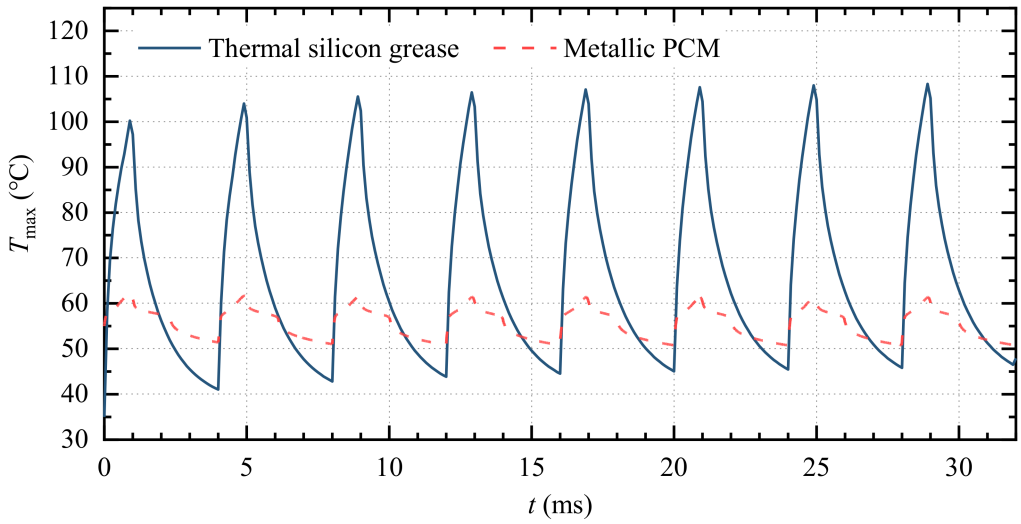


Figure 15. The transient response under heat pluses of the thermal silicon grease.

3.3. Comparison of the Current Study with Other Existing Numerical Studies

Numerous numerical studies have been established to demonstrate the potential of heat sinks incorporated with metallic PCMs. Table 3 compares the current study with other existing numerical studies, including the metallic PCMs, co-design of PCMs and heat sinks, and numerical models. It can be seen that most of the existing designs combine PCMs with finned heat sinks, and only the heat transfer and melting processes were considered in the numerical models. For the conjugate heat transfer process involving convection heat transfer, the heat transfer coefficient was calculated by correlation or set to constant. In the current study, a thin-layer metallic PCM is embedded between the contact surface of chips and the impingement heat sink, and the conjugated heat transfer processes involving the convection heat transfer of fluid, heat conduction of solid structures and melting of

PCMs are modeled. The above discussions of the simulation results have demonstrated the effectiveness of the thermal performance of a jet impingement heat sink with a metallic PCM for the thermal management of millisecond-pulsed heat sources, reflecting the innovation of this work.

Table 3. Comparison of the current study with other existing numerical studies.

Author	Metallic PCM	Co-Design of PCM and Heat Sink	Numerical Model
DW Yoo et al. [19]	50Bi/27Pb/13Sn/10Cd	Fill the fan cooled external plate fin heat sink with PCM	PCM melting under forced convection was modeled using the enthalpy–porosity approach, and the heat transfer coefficient on the air-cooled channel surfaces was calculated by correlation.
Gaofeng Hao et al. [20]	Vrycul TP-III	Integrate PCM into IGBT molybdenum plate	Only the heat transfer and PCM melting processes were involved, and the apparent heat capacity method was used to model phase transition processes.
Ahmed et al. [45]	50Bi/27Pb/13Sn/10Cd	Thin film metallic PCM in direct contact with the chip	One dimensional model and the enthalpy method were used to model phase transition processes.
Xiaohu Yang et al. [21]	31.6Bi/48.8In/19.6Sn	Fill the internal finned heat sink with PCM	PCM melting processes were modeled using the enthalpy–porosity method, and the natural convection heat transfer coefficient of the heat sink outer wall was set to constant.
Xiaohu Yang et al. [22]	49Bi/21In/18Pb/12Sn	Fill the internal finned heat sink with PCM	Only the heat transfer and PCM melting processes were involved, and the enthalpy–porosity method was used to model phase transition processes.
Present work	49Bi/21In/18Pb/12Sn	Embed PCM into the interface between the chips and the jet impingement heat sink	The *k*-ω turbulence model and the apparent heat capacity method were used to model the conjugated heat transfer of confined jet impingement cooling and PCM melting.

4. Conclusions

In this paper, a heat sink combining the confined jet impingement with metallic phase change material (PCM) was proposed for the thermal management of millisecond-pulsed heat sources. A transient model was established to simulate the conjugated heat transfer and the main outcomes from the present work are summarized as follows.

(1) Under the same volumetric flow rate of the cooling medium, the heat transfer of jet impingement can be enhanced with the decrease in jet diameter and jet height, but the pressure drop increases dramatically. For a jet diameter of 2 mm and impingement height of 2 mm, the maximum surface temperature on a 3 × 3.5 mm^2 surface of a constant heat flux of 150 W/cm^2 can be cooled to 62.2 °C with a coolant inlet temperature of 35 °C.

(2) Under the heat pulses with a peak heat flux of 600 W/cm^2 and duration of 1 ms per 4 ms, the temperature fluctuates in the same period as the heat pulses, and the maximum temperature is increased to 66.9 °C for jet impingement cooling. After adding a thin layer of metallic PCM, the maximum temperature can be reduced to 61.5 °C.

(3) The PCM thickness has a significant influence on the cooling performance. Results show that the maximum temperature can be maintained around the phase change temperature only if the melted PCM during the heating period can be completely solidified within heat pulse intervals, suggesting that a thickness smaller than 0.1 mm is appropriate.
(4) The heat pluses' peak heat flux and duty cycle also have effects on the buffer performance of PCM. Results show that low peak heat flux and large duty cycle pulse heating can take full advantage of metallic PCMs.
(5) Compared to the thermal silicon grease, metallic PCM can achieve a lower temperature and a smaller amplitude of fluctuations under pulses, showing a better thermal contact performance.

Author Contributions: Conceptualization, L.C. and Y.H.; methodology, L.C. and Q.W.; software, L.C. and Q.W.; validation, L.C. and Q.W.; formal analysis, L.C. and Q.W.; investigation, Q.W. and Y.S.; resources, L.C., Q.W. and Y.H.; data curation, Q.W.; writing—original draft preparation, L.C. and Q.W.; writing—review and editing, L.C. and Y.H.; visualization, L.C. and Q.W.; supervision, L.C. and Y.H.; project administration, L.C. and Y.H.; funding acquisition, L.C. and Y.H. All authors have read and agreed to the published version of the manuscript.

Funding: This study was supported by the National Natural Science Foundation of China (52176020) and the Youth Innovation Team of Shaanxi Universities.

Institutional Review Board Statement: Not applicable.

Informed Consent Statement: Not applicable.

Data Availability Statement: Not applicable.

Conflicts of Interest: The authors declare no conflict of interest.

Nomenclature

C_p	specific heat capacity ($J \cdot kg^{-1} \cdot K^{-1}$)
d	jet diameter (mm)
H	jet height (mm)
h	heat transfer coefficient ($W \cdot m^{-2} \cdot K^{-1}$)
k	thermal conductivity ($W \cdot m^{-1} \cdot K^{-1}$)
L	latent heat (J/kg)
Nu	Nusselt number
Nu_0	stagnation point Nusselt number
ΔP	pressure drop (Pa)
Q_V	volumetric flow rate (L/min)
q''	heat flux (W/cm^2)
Re	Reynold number
T	temperature (°C)
T_m	mean temperature of the phase change (°C)
t	time (ms)
u	velocity (m/s)
Greek symbols	
δ	the thickness of metallic PCM (mm)
ρ	density (kg/m^3)
γ	average phase change percentage (%)
θ	liquid fraction
Superscripts	
ave	average
max	maximum

References

1. Garimella, S.V.; Fleischer, A.S.; Murthy, J.Y.; Keshavarzi, A.; Prasher, R.; Patel, C.; Bhavnani, S.H.; Venkatasubramanian, R.; Mahajan, R.; Joshi, Y.; et al. Thermal Challenges in Next-Generation Electronic Systems. *IEEE Trans. Components Packag. Technol.* **2008**, *31*, 801–815. [CrossRef]
2. Huang, Y.-C.; Hsu, H.-C. Selective Laser Melting Heat Sinks under Jet Impingement Cooling for Heat Dissipation of Higher Light Output LED Lighting in a Limited Space. *Appl. Sci.* **2020**, *10*, 3898. [CrossRef]
3. Zhu, L.Y.; Cao, J.G.; Dong, L.N. Review on Jet Impingement Technology for Spacecraft High-Heat-Flux Removal. *Aerosp. Shanghai* **2016**, *33*, 106–112. [CrossRef]
4. Garimella, S.V.; Nenaydykh, B. Nozzle-geometry effects in liquid jet impingement heat transfer. *Int. J. Heat Mass Transf.* **1996**, *39*, 2915–2923. [CrossRef]
5. Robinson, A.; Schnitzler, E. An experimental investigation of free and submerged miniature liquid jet array impingement heat transfer. *Exp. Therm. Fluid Sci.* **2007**, *32*, 1–13. [CrossRef]
6. Garimella, S.V.; Rice, R.A. Confined and Submerged Liquid Jet Impingement Heat Transfer. *J. Heat Transf.* **1995**, *117*, 871–877. [CrossRef]
7. Womac, D.J.; Incropera, F.P.; Ramadhyani, S. Correlating equations for impingement cooling of small heat sources with multiple circular liquid jets. *ASME J. Heat Transf.* **1994**, *116*, 482–486. [CrossRef]
8. Garimella, S.V. Heat transfer and flow fields in confined jet impingement. *Annu. Rev. Heat Transf.* **2000**, *11*, 413–494. [CrossRef]
9. Nguyen, C.T.; Galanis, N.; Polidori, G.; Fohanno, S.; Popa, C.V.; Le Bechec, A. An experimental study of a confined and submerged impinging jet heat transfer using Al2O3-water nanofluid. *Int. J. Therm. Sci.* **2009**, *48*, 401–411. [CrossRef]
10. Zhang, D.; Qu, H.; Lan, J.; Chen, J.; Xie, Y. Flow and heat transfer characteristics of single jet impinging on protrusioned surface. *Int. J. Heat Mass Transf.* **2013**, *58*, 18–28. [CrossRef]
11. Sathik, M.; Jet, T.K.; Gajanayake, C.J.; Simanjorang, R.; Gupta, A.K. Comparison of power cycling and thermal cycling effects on the thermal impedance degradation in IGBT modules. In Proceedings of the 41st Annual Conference of the IEEE Industrial Electronics Society, Yokohama, Japan, 9–12 November 2015. [CrossRef]
12. Liu, Z.; Qin, S.; Chen, X.; Chen, D.; Wang, F. PDMS-PDMS Micro Channels Filled with Phase-Change Material for Chip Cooling. *Micromachines* **2018**, *9*, 165. [CrossRef]
13. Iradukunda, A.-C.; Vargas, A.; Huitink, D.; Lohan, D. Transient thermal performance using phase change material integrated topology optimized heat sinks. *Appl. Therm. Eng.* **2020**, *179*, 115723. [CrossRef]
14. Pal, D.; Joshi, Y.K. Application of Phase Change Materials to Thermal Control of Electronic Modules: A Computational Study. *J. Electron. Packag.* **1997**, *119*, 40–50. [CrossRef]
15. Liu, J.; Deng, Z.-S.; He, Z.-Z. Art and Science Towards Noiseless Driving of Liquid Metal for Advanced Thermal Management of High Heat Flux Device. In *International Electronic Packaging Technical Conference and Exhibition*; American Society of Mechanical Engineers: San Francisco, CA, USA, 2015. [CrossRef]
16. Xiaohu, Y.; Liu, J. Advanced liquid metal cooling: Historical developments and research frontiers. *Sci. Technol. Rev.* **2018**, *36*, 54–66.
17. Boteler, L.; Fish, M.; Berman, M.; Wang, J. Understanding Trade-Offs of Phase Change Materials for Transient Thermal Mitigation. In Proceedings of the 2019 18th IEEE Intersociety Conference on Thermal and Thermomechanical Phenomena in Electronic Systems (ITherm), Las Vegas, NV, USA, 28–31 May 2019; pp. 870–877.
18. Cai, Y.; Hong, B.-H.; Wu, W.-X.; Wang, W.-W.; Zhao, F.-Y. Active cooling performance of a PCM-based thermoelectric device: Dynamic characteristics and parametric investigations. *Energy* **2022**, *254*, 124356. [CrossRef]
19. Yoo, D.-W.; Joshi, Y. Energy Efficient Thermal Management of Electronic Components Using Solid–Liquid Phase Change Materials. *IEEE Trans. Device Mater. Reliab.* **2004**, *4*, 641–649. [CrossRef]
20. Hao, G.; Zhou, L.; Ren, H.; Ran, L.; Xie, B. Study on thermal buffering effect of phase change material on press-pack IGBT. *Int. J. Heat Mass Transf.* **2020**, *154*, 119584. [CrossRef]
21. Yang, X.-H.; Tan, S.-C.; Ding, Y.-J.; Wang, L.; Liu, J.; Zhou, Y.-X. Experimental and numerical investigation of low melting point metal based PCM heat sink with internal fins. *Int. Commun. Heat Mass Transf.* **2017**, *87*, 118–124. [CrossRef]
22. Yang, X.-H.; Tan, S.-C.; He, Z.-Z.; Zhou, Y.-X.; Liu, J. Evaluation and optimization of low melting point metal PCM heat sink against ultra-high thermal shock. *Appl. Therm. Eng.* **2017**, *119*, 34–41. [CrossRef]
23. Yang, X.-H.; Tan, S.-C.; He, Z.-Z.; Liu, J. Finned heat pipe assisted low melting point metal PCM heat sink against extremely high power thermal shock. *Energy Convers. Manag.* **2018**, *160*, 467–476. [CrossRef]
24. Shamberger, P.J.; Bruno, N.M. Review of metallic phase change materials for high heat flux transient thermal management applications. *Appl. Energy* **2020**, *258*, 113955. [CrossRef]
25. Muratore, C.; Aouadi, S.; Voevodin, A. Embedded phase change material microinclusions for thermal control of surfaces. *Surf. Coatings Technol.* **2012**, *206*, 4828–4832. [CrossRef]
26. Ollier, E.; Soupremanien, U.; Remondière, V.; Dijon, J.; Le Poche, H.; Seiler, A.; Lefevre, F.; Lips, S.; Kinkelin, C.; Rolland, N.; et al. Thermal management of electronic devices by composite materials integrated in silicon. *Microelectron. Eng.* **2014**, *127*, 28–33. [CrossRef]
27. Sponagle, B.; Groulx, D.; White, M. Experimental Evaluation of a Latent Heat Storage Module with a Heat Spreader for Thermal Management of a Tablet Computer. *Appl. Sci.* **2021**, *11*, 3983. [CrossRef]

28. Maranda, S.; Sponagle, B.; Worlitschek, J.; Groulx, D. Experimental Investigation of Thin PCM Packages and Thermal Spreader for Thermal Management of Portable Electronic Devices. *Appl. Sci.* **2019**, *9*, 4613. [CrossRef]
29. Potthast, F.; Laschefski, H.; Mitra, N.K.; Biswas, G. Numerical investigation of flow structure and mixed convection heat transfer of impinging radial and axial jets. *Numer. Heat Transf. Part A Appl.* **1994**, *26*, 123–140. [CrossRef]
30. Revill, B.K. Chapter 9—Jet mixing. In *Mixing in the Process Industries*; Harnby, N., Edwards, M.F., Nienow, A.W., Eds.; Butterworth-Heinemann: Oxford, UK, 1992; pp. 159–183.
31. Tao, W. *Numerical Heat Transfer*, 2nd ed.; Xi'an Jiaotong University Press: Xi'an, China, 2001.
32. Muhammad, A.; Selvakumar, D.; Wu, J. Numerical investigation of laminar flow and heat transfer in a liquid metal cooled mini-channel heat sink. *Int. J. Heat Mass Transf.* **2020**, *150*, 119265. [CrossRef]
33. Wilcox, D.C. *Turbulence Modeling for CFD*; DCW Industries, Inc.: La Canada, CA, USA, 1998.
34. Khattari, Y.; El Rhafiki, T.; Choab, N.; Kousksou, T.; Alaphilippe, M.; Zeraouli, Y. Apparent heat capacity method to investigate heat transfer in a composite phase change material. *J. Energy Storage* **2020**, *28*, 101239. [CrossRef]
35. El Ouali, A.; Khattari, Y.; Lamrani, B.; El Rhafiki, T.; Zeraouli, Y.; Kousksou, T. Apparent heat capacity method to describe the thermal performances of a latent thermal storage system during discharge period. *J. Energy Storage* **2022**, *52*, 104960. [CrossRef]
36. COMSOL AB. Heat Transfer Module User's Guide. In *COMSOL Multiphysics®v. 5.5*; COMSOL AB: Stockholm, Sweden, 2019; pp. 77–80.
37. Desai, A.; Singh, V.K.; Bhavsar, R.R. Numerical investigation of pcm based thermal control module for space applications. In Proceedings of the 24th National and 2nd International ISHMT-ASTFE Heat and Mass Transfer Conference (IHMTC-2017), Hyderabad, India, 27–30 December 2017.
38. Manikandan, S.; Selvam, C.; Poddar, N.; Pranjyal, K.; Lamba, R.; Kaushik, S. Thermal management of low concentrated photovoltaic module with phase change material. *J. Clean. Prod.* **2019**, *219*, 359–367. [CrossRef]
39. Mazloum, S.; Awad, S.; Allam, N.; Aboumsallem, Y.; Loubar, K.; Tazerout, M. Modelling plastic heating and melting in a semi-batch pyrolysis reactor. *Appl. Energy* **2021**, *283*, 116375. [CrossRef]
40. Pan, A.-G.; Wang, J.-B.; Zhang, X.-J.; Cao, X.-B. Experimental Research of Electronic Devices Thermal Control Using Metallic Phase Change Materials. *J. Harbin Inst. Technol.* **2014**, *21*, 113–121.
41. Li, C.-Y.; Garimella, S.V. Prandtl-number effects and generalized correlations for confined and submerged jet impingement. *Int. J. Heat Mass Transf.* **2001**, *44*, 3471–3480. [CrossRef]
42. Shishkin, R.A. Investigation of the influence of submicron spherical diamond particles and silicon whiskers on the thermal conductivity of thermal greases. In *AIP Conference Proceedings*; AIP Publishing: Melville, NY, USA, 2022; Volume 2632, p. 020022. [CrossRef]
43. Hansson, J.; Nilsson, T.M.J.; Ye, L.; Liu, J. Novel nanostructured thermal interface materials: A review. *Int. Mater. Rev.* **2018**, *63*, 22–45. [CrossRef]
44. Wang, X.; Lu, C.; Rao, W. Liquid metal-based thermal interface materials with a high thermal conductivity for electronic cooling and bioheat-transfer applications. *Appl. Therm. Eng.* **2021**, *192*, 116937. [CrossRef]
45. Hamed, A.; Ndao, S. Modeling of writable thin film liquid metal phase change material for electronics cooling. In Proceedings of the 2017 16th IEEE Intersociety Conference on Thermal and Thermomechanical Phenomena in Electronic Systems (ITherm), Orlando, FL, USA, 30 May–2 June 2017; pp. 1062–1068.

Disclaimer/Publisher's Note: The statements, opinions and data contained in all publications are solely those of the individual author(s) and contributor(s) and not of MDPI and/or the editor(s). MDPI and/or the editor(s) disclaim responsibility for any injury to people or property resulting from any ideas, methods, instructions or products referred to in the content.